RSC Advances

PAPER

View Article Online
View Journal | View Issue

Cite this: *RSC Adv.*, 2014, **4**, 61771

Nanosized Pt-containing Al_2O_3 as an efficient catalyst to avoid coking and sintering in steam reforming of glycerol†

Davi C. Carvalho,[a] Helvio S. A. Souza,[a] Josué M. Filho,[b] Elisbete M. Assaf,[c] Vivian V. Thyssen,[c] Adriana Campos,[d] E. Padron Hernandez,[e] Ramon Raudel[e] and Alcineia C. Oliveira*[a]

Received 5th September 2014
Accepted 5th November 2014

DOI: 10.1039/c4ra09895a

www.rsc.org/advances

The action of nanosized Pt-containing Al_2O_3 catalysts to avoid coking and sintering was studied in steam reforming of glycerol. The solids exhibited almost 100% conversion toward syngas produced at a suitable water to glycerol ratio. Depending on the promoter, a drastic drop in hydrogen yield was observed due to coking and sintering effects. Spent catalyst characterizations by Raman, HRTEM, XRD, TG and SEM-EDS as well as textural property techniques showed that coking, rather than sintering, was the main cause that determined the low hydrogen selectivity of nanosized Pt-containing Al_2O_3 with La_2O_3 or ZrO_2. In contrast, coking did not cover the active sites of Pt-containing Al_2O_3 with MgO or CeO_2. Thus, steam suppressed carbon deposition and improved the nanosized Pt/MgO–Al_2O_3 catalyst stability in the steam reforming of glycerol.

1. Introduction

Glycerol is produced as a byproduct of biodiesel production. Due to environmental concerns, it is highly desired to develop alternatives for valorization of crude glycerol. Steam reforming of glycerol to hydrogen or for syngas production is one of the most attractive options to make use of glycerol, as it can stoichiometrically produce up to 7 mol of hydrogen from 1 mol of the trialcohol (eqn (1)).

$$C_3H_8O_3 + 3H_2O \rightleftharpoons 7H_2 + 3CO_2 \; \Delta H_{298K} = +128 \text{ kJ mol}^{-1} \quad (1)$$

Although processes mainly based on pyrolysis, autothermal reforming, supercritical water reforming, photo-reforming and aqueous phase reforming of glycerol are potentially suitable for hydrogen production over the conventional steam reforming reaction, the amount of hydrogen produced and its selectivity are less based on thermodynamic analyses.[1–4]

So far, to take full advantage of the benefits of hydrogen as a clean energy carrier, economically viable and environmentally friendly low carbon emitting, catalysts for producing hydrogen are needed. In order to fulfil this, detailed studies of glycerol steam reforming using different catalysts in a fixed-bed reactor have been conducted.[2–7] It should be highlighted that due to the high water to organic ratio and the high specific heat of water, the production of hydrogen is favoured. Moreover, upon using steam-to-glycerol ratio in the range of 9–12 and reaction temperature at around 600–700 °C, the steam reforming of glycerol is likely.[1,5] Thus, nickel–cobalt-based catalysts and noble metal ones are succeeded in steam reforming of glycerol to catalyze most carbohydrates reforming reactions and reforming of methanol, ethanol as well as glycerol, due to chemical similarity of the feedstock.[8–16] In general, one of the reasons of choice between Pt- and Ni-based catalysts is the resistance to phase transformation and tolerance against sulfur compounds, rather than their catalytic activity. However, at least in the case of steam reforming of glycerol, platinum-based catalysts appear to be more efficient than Ni ones, which suffer coking more than Pt-based ones and have shorter life.[1,13]

In this sense, glycerol has ability to decompose over the Pt surface through O–H, C–C and C–H bond dissociations to produce syngas.[1] Indeed, Pt surface also has low activity toward C–O bond dissociations, as observed throughout the Fischer–Tropsch and methanation reactions to produce hydrogen. Pt presence also avoids the water gas shift reaction because of the lack of catalytic sites required to activate water.[1,13]

---

[a] *Universidade Federal do Ceará, Campus do Pici-Bloco 940, Fortaleza, Ceará, Brazil. E-mail: alcineia@ufc.br; Fax: +55-85-3366-90-51 ext. 9982; Tel: +55-85-3366-90-51 ext. 9982*

[b] *Universidade Federal do Ceará, Departamento de Física, Bloco 920, Fortaleza, Ceará, Brazil. Fax: +55-85-3366-94-83; Tel: +55-85-3366-94-83*

[c] *Instituto de Química de São Carlos, Universidade de São Paulo, Av. Trabalhador Sãocarlense, 400, 13560-970 São Carlos, SP, Brazil*

[d] *CETENE, Cidade Universitária, Av. Prof. Luiz Freire, Recife, Pernambuco, Brazil. Fax: +55-81-33347224; Tel: +55-81-33347224*

[e] *Universidade Federal de Pernambuco, Departamento de Física – CCEN, Cidade Universitária, Av. Professor Luiz Freire, S/N, 50670-901, Recife, PE, Brazil. Tel: +55-81-91778360*

† Electronic supplementary information (ESI) available. See DOI: 10.1039/c4ra09895a

Concerning the carries, Pt supported on Al_2O_3 catalysts have been widely investigated in steam reforming reactions due to its ability to preventing Pt from incorporation to γ-Al_2O_3 phase, stabilizing Pt^o particles and reducing support acidity.[13] Nevertheless, even with a better performance, there is always a need for improving the Pt-based catalysts and also provide the reasons for the deactivation of the solids. As steam reforming of glycerol is endothermic and needs heat to work, this is a harsh reaction condition to operate and would damage the catalysts.[1] It is also recognized that the catalytic activity may be enhanced by modifying Al_2O_3 with a small amount of La_2O_3, CeO_2, MgO or ZrO_2.[12] This can improve the catalytic activity and stability of the solids for steam reforming of glycerol reaction. However, coking blocks active sites and increases the amounts of light byproducts such as methane and ethylene, among others. In addition, supports possessing acid properties exhibit low activity to gaseous products and form lateral products owing to dehydration and condensation reactions. Whereas solids prepared through supports with neutral properties allow to obtain catalysts with excellent activity levels to gaseous products in steam reforming of glycerol, high selectivity to hydrogen and stability during long terms stability runs as well.[1]

Recently, we have reported a low temperature process for the dry reforming of methane (DRM) to synthesis gas over nanostructured Pt-based catalysts.[17] In fact, the deactivation of the catalysts in reason of carbonaceous residues deposition is inevitable in DRM reaction. However, the resistance exhibited by the nanostructured solids against sintering and phase transformation affords expectances to maximize hydrogen production with negligible coke deposition in steam reforming of glycerol reaction.

Thus, the aim of this study is to examine hydrogen production from steam reforming of glycerol using nanostructured catalysts. The study comprises the role played by the structure of the nanostructured oxides to avoid catalysts deactivation. Up to now, it is possible for the reforming process to operate in relatively low temperatures in order to reduce deactivation upon using such solids.

The spent catalysts were characterized by the chemical analysis, nitrogen adsorption desorption measurements, XRD, Raman spectroscopy, HRTEM, TG, and SEM-EDS. The GC-MS are applied to analyze the products from steam reforming of glycerol.

2. Experimental

2.1. Catalyst preparation

Catalyst based on MeO_x–Al_2O_3, in which Me = MgO, CeO_2, La_2O_3 or ZrO_2 were synthesized according to the previous works.[14,15,17] The detailed procedure was described previously.[17] The MeO_x/Al_2O_3 ratios were about 20 : 80 wt%.

Briefly, mesoporous MeO_x–Al_2O_3 supports were impregnated with hexachloroplatinic acid (H_2PtCl_6) solution using 1 g of each support and the mixture was stirred at 40 °C for 2 h. The solid was subsequently dried and calcined for 3 h at 350 °C in flowing air (1 °C min^{-1}). The mesoporous PtO_x/MgO–Al_2O_3, PtO_x/CeO_2–Al_2O_3, PtO_x/CeO_2–La_2O_3 and PtO_x/ZrO_2–Al_2O_3 catalysts were obtained. The nominal amount of Pt was about 1 wt%.

The physicochemical properties of the aforesaid fresh catalysts were deeply investigated in our previous work.[17]

2.2. Characterizations of the spent solids

X-ray powder diffraction was used to identify the phases formed after the catalytic test. A from X'Pert ProMPD X-ray diffraction equipment having an X-ray generator with CuKα radiation by using 40 kV and 40 mA was used for the measurements. The solids were scanned in the range $2\theta = 3$–$80°$. XRD patterns were compared with those of JCPDS database.

BET surface area, pore volume, and average pore diameter for spent solids were derived from nitrogen adsorption isotherms measured at −196 °C in a Micromeritics ASAP 2000. Before the measurement, each sample was degassed at 120 °C under vacuum for 10 h to remove the adsorbed moisture on the catalyst surface. The pore size distributions were calculated from the desorption branch of isotherms using Barrett–Joyner–Halenda method (BJH).

Laser Raman spectroscopy measurements analyses were performed at room temperature in a LabRam spectrometer (Jobin-Yvon). The emission line at 532 nm from an argon ion laser was focused onto the samples using the macroscopic configuration and samples were examined at low laser power (2 mW) to avoid damage due to laser heating. The device was coupled to an Olympus confocal microscope and a 100 times objective lens was used for simultaneous illumination and collection. Additionally, the device was equipped with a CCD with the detector cooled to about −10 °C. Ten accumulated spectra were obtained in each spectral range and the spectral resolution was 3 cm^{-1} in the 5–2000 cm^{-1} range.

High resolution transmission electron (HRTEM) and transmission electron (TEM) micrographs of spent solids were obtained in a FEI Tecnai20 G2 200 kV electron microscope to observe morphology of carbon deposits and particle size. Selected catalysts were ultrasonically dispersed in ethanol and a drop of the suspension was then applied onto clean copper grids and dried at room temperature.

Scanning electron microscopy (SEM) equipped with an energy dispersive analysis system (EDS) measurements were used to study the surface morphology and the element mapping of surface composition of the catalysts. The measurements were conducted on a TESCAN VEGA XMU electron microscope equipped with an EDS Bruker QUANTAX system coupled to the SEM microscope, using an acceleration voltage of 20 kV. Previously, the solids were deposited on an aluminium sample holder and sputtered with gold and then SEM measurements were conducted.

Amounts of carbon deposits were obtained by thermogravimetric analysis (TG) coupled to differential scanning calorimetry (DSC) apparatus in a Netzsch STA 409 PC/PG equipment coupled to a Bruker Tensor 27 IR instrument, under air stream between 50 and 1000 °C at a rate of 10 °C min^{-1}.

2.3. Activity testing

Catalytic tests in steam reforming of glycerol were performed in a quartz fixed-bed reactor with 39 cm and 1 cm of inner diameter. Blank runs were performed prior to the catalytic reactions and conversion of glycerol values was negligible. Typically, 150 mg catalysts were sandwiched by quartz wool and packed in the reactor and activated *in situ* under a gas mixture of hydrogen and nitrogen at 600 °C for 1 h with hydrogen flow of 30 cm^3 min^{-1}. Thereafter, the system was purged flowing nitrogen while it reached the reaction temperature. A thermocouple was inserted into the centre of the catalytic bed to monitor the reaction temperature. A mixture of water to glycerol ratio of 9 : 1 was fed into the reactor through a high-precision pump. The cold trap contained the liquid products which were analysed without preliminary extraction or separation using a gas chromatograph (Shimadzu) equipped with a FID detector and HP5 capillary column and operating between 35 and 250 °C with hydrogen as carrier gas.

Gaseous samples were analyzed using gas chromatograph Varian Chrompack GC-3800 using hydrogen as carrier gas. The chromatograph was equipped with two packed columns, namely Porapak-N and Molecular Sieve 13X and operates between 40 and 80 °C with a carrier gas of He and N_2, respectively, flowing at 10 mL min^{-1}. The carbon balances were about 5% in errors.

3. Results and discussion

3.1. Catalytic performances of the solids in steam reforming of glycerol

Characterizations of the fresh catalysts have been described in detail in our previous paper that contains a summary of the main features of the catalysts screened.[17]

Conversion values in steam reforming of glycerol are shown in Table 1.

The catalysts exhibit high efficiency in steam reforming of glycerol with optimized reaction conditions along of 300 h time on stream. According to the table, glycerol conversion is maximum for the $PtO_x/MgO–Al_2O_3$. It is evident that the other catalysts show significant performances with respect to that $PtO_x/MgO–Al_2O_3$, except for $PtO_x/CeO_2–La_2O_3$ whose performance is the lowest among the solids studied. The H_2/CO_2 ratios are indicative of the yields of gaseous products. The findings states that the theoretical ratios for glycerol steam reforming is close to 2.3 (mol/mol).[1,7] Thus, the H_2/CO_2 ratio obtained are similar and agree with those predicted theoretically and it may suggest an optimal behaviour for steam reforming of glycerol. On the other hand, values of H_2/CO ratio between 5.0 and 7.0 indicate the presence of side reactions such as glycerol decomposition to hydrogen and carbon and reverse water gas shift (RWGS) reaction, among others, as shown elsewhere.[18]

Fig. 1 shows plots of yields and selectivity of the products obtained *versus* time on stream.

Both gaseous and liquid products are obtained by chromatogram analyses over all catalysts. The hydrogen yield is about 7.0 within *ca.* 5 h over $PtO_x/ZrO_2–Al_2O_3$ due to the complete steam reforming (Fig. 1a) leading to similar production of hydrogen, as that observed for $PtO_x/MgO–Al_2O_3$. Similar results are seen for gas compositions over the aforesaid catalyst at space velocity as low as 0.25 h^{-1} (Fig. 1b). The elevated hydrogen production is believed to be from the well dispersion of Pt on the support, as previously observed.[17] However, sintering of particles from $PtO_x/ZrO_2–La_2O_3$ and $PtO_x/MgO–Al_2O_3$ at the expense of faster coking rates can further explain these results. Moreover, relatively low amounts of CO_2 and CO are produced over these solids, owing to the reverse water gas shift (RWGS) reaction occurrence whereas CH_4 production is negligible.

Hydrogen yields for CeO_2-containing catalysts achieve values below to 5 comparing with the other catalysts. Such an effect can be expected to be resulted from the different types of interaction of CeO_2 with La_2O_3 and Al_2O_3. The role of CeO_2-in tuning structural properties could be a result of presence of a stable phase *e.g.*, $CeAlO_3$ combined with its high surface area, which promote the dispersion of the Pt^o nanoparticles, as observed for dry reforming of methane.[17] This not the case of the interaction between CeO_2 with La_2O_3, whose a huge mismatch between fast carbon deposition (latter shown in spent catalysts characterizations) and reduction/oxidation cycles of CeO_2 as well as a mobile surface oxygen species transferred to Pt are observed.[19] The yields of CO and CO_2 are rather limited to the impurity amounts.

Although the conversions of glycerol over $PtO_x/ZrO_2–Al_2O_3$ and $PtO_x/MgO–Al_2O_3$ are slightly higher than those Ce-containing catalysts, the formers have very close H_2 selectivity (about 55%, Fig. 1a). The hydrogen selectivity decreases with

Table 1 Catalytic activity of the solids in steam reforming of glycerol reaction. Reaction conditions: reaction temperature at 600 °C, water to glycerol ratio of 9 : 1 and catalyst mass of 0.15 g during 5 h of reaction. The physicochemical characterizations of the catalysts studied after the aforesaid catalytic test condition[a]

Catalyst	Glycerol conversion (%)	H_2/CO_2 ratio	H_2/CO ratio	Phases detected after the catalytic test	Particle sizes[b] (nm)	Sg[c] (m^2 g^{-1})	Vp[c] (cm^3 g^{-1})	Dp[c] (nm)
$PtO_x/CeO_2–Al_2O_3$	97.0	2.8	6.3	CeO_2; γ-Al_2O_3; $CeAlO_3$; C	5	83	0.11	4.5
$PtO_x/ZrO_2–Al_2O_3$	97.0	2.9	5.2	ZrO_2; γ-Al_2O_3	35	73	0.11	2.8
$PtO_x/MgO–Al_2O_3$	100	2.7	7.5	MgO; γ-Al_2O_3; $MgAl_2O_4$; C	15	152	0.20	4.0
$PtO_x/CeO_2–La_2O_3$	96.0	2.6	7.0	CeO_2; γ-Al_2O_3; La_2O_3; C	30	103	0.14	3.1

[a] XRD. [b] TEM. [c] Nitrogen adsorption–desorption measurements.

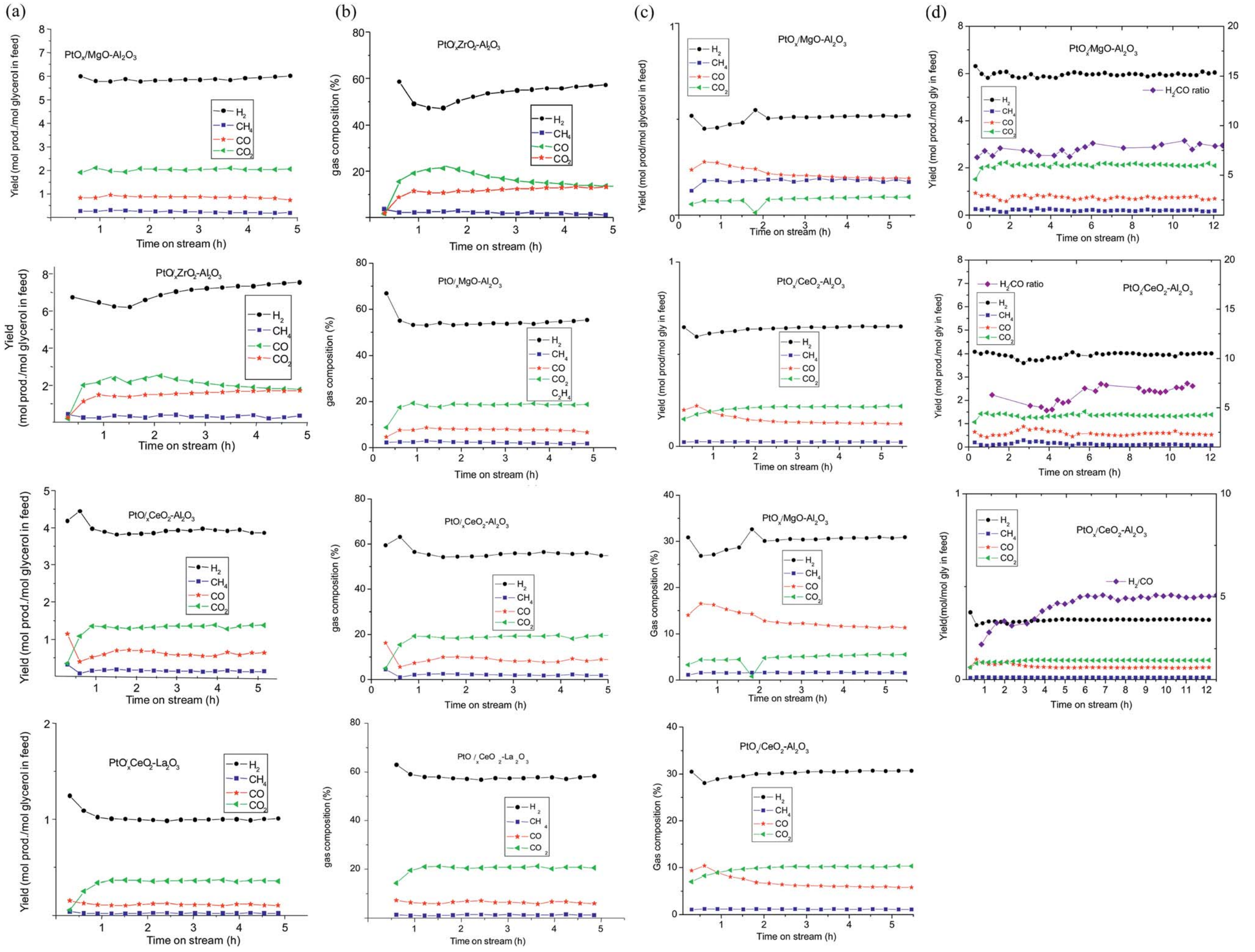

Fig. 1 Short-term catalytic runs over the catalysts studied. (a) Yield of gaseous products formed (b) Selectivity to the products obtained. Reaction conditions: fixed temperature (600 °C), time of 5 h, water to glycerol ratio of 9 and space velocity of 0.25 h^{-1} (c) yield of gaseous products formed and selectivity to the products obtained. Reaction conditions: fixed temperature (600 °C), time 5 h and water to glycerol ratio of 9 and space velocity of 0.5 h^{-1} (d) long term stability runs over the $PtO_x/MgO–Al_2O_3$ and $PtO_x/CeO_2–Al_2O_3$ at 600 °C, water to glycerol ratio of 9 : 1 and space velocities of 0.25 and 0.5 h^{-1} as well.

time on stream in reason of hydrogen in water favouring the hydrogen production *via* Water Gas Shift (WGS) reaction over $PtO_x/ZrO_2–Al_2O_3$ at the beginning of the reaction and a further stabilization of hydrogen production is observed. The same linearity is shown for $PtO_x/MgO–Al_2O_3$ and hydrogen selectivity is always 55%, suggesting that the mechanisms of hydrogen production are the same for these two catalysts. Meanwhile, the selectivities of CO_2 and CO experience an increase at the beginning of the reaction and subsequently drop, being quite low at the end of the catalytic runs. This observation also suggests that possible phase transformations may be occurred over $PtO_x/ZrO_2–Al_2O_3$ while MgO modification on PtO_x/Al_2O_3, led to similar changes in H_2 due to sintering (further shown by TEM and XRD). Moreover, very low detectable amounts of CO, CH_4 and CO_2 (below 20%) and undesired C_2H_4 can be observed in the short-term stability run over both $PtO_x/ZrO_2–Al_2O_3$ and $PtO_x/MgO–Al_2O_3$, demonstrating that the hydrogen production is facilitated over these solids.

Both $PtO_x/CeO_2–Al_2O_3$ and $PtO_x/CeO_2–La_2O_3$ demonstrate that the H_2 selectivity has a plateau by *ca.* 54% within *ca.* 5 h on stream whereas CO_2 and CO selectivities are 20%. Despite the low hydrogen yield, $PtO_x/CeO_2–La_2O_3$ has elevated selectivity to the gaseous products. This important aspect implies the CeO_2 combined with La_2O_3 facilitate the formation of CO_2 and water by WGS reaction providing a pathway for removing adsorbed CO from the Pt surface and thus inhibiting reforming reactions by blocking surface sites.[20] In addition, the elevated C_2H_4 selectivity indicates that coking caused by polymerization is not beneficial for hydrogen production.

In case of condensate liquid effluents, analyses show that the small amounts of byproducts are formed. There are formic and propionic acids, acetone, diols, acetone, ethanol, glycidol, sorbitol, propylene glycol and dioxolanes, which are detected in the condensate.

Traces of higher molecular weight condensation products are also found over $PtO_x/CeO_2–Al_2O_3$ and $PtO_x/CeO_2–La_2O_3$, confirming the existence of coke precursor over these solids.

Studies lead on $PtO_x/CeO_2–Al_2O_3$ and $PtO_x/MgO–La_2O_3$ reveal that the yield of the products and selectivity decay for much longer space velocity (up to 0.25 h^{-1}, Fig. 1c). Comparisons between Fig. 1b and c show the effect of space velocity process variable over product distribution and glycerol conversion. As it can be seen, lower glycerol conversion and hydrogen yield as well as change of CO product distribution (H_2/CO_2 ratio of 6.0) are observed with increase in space velocity. Besides, the yields of methane and CO_2 are also negligible under these conditions. These behaviors suggest that CO seems to be formed by consecutive reactions such as RWGS reaction. Thermodynamic analyses for steam reforming of glycerol based on non-stoichiometric approach shows that the hydrogen yield value at equilibrium is found to be 6.86 with dilute feed system containing 10 wt% of glycerol.[9] Thus, the hydrogen yield is far from equilibrium using space velocity higher than 0.25 h^{-1} and lower glycerol feed concentration (*i.e.* 10 wt% glycerol).

Extended tests over longer periods up to 12 h results are shown in Fig. 1d. The hydrogen production on $PtO_x/MgO–Al_2O_3$ is particularly high, showing approximately 6 mol mol^{-1} of glycerol supplied greater yield than on $PtO_x/CeO_2–Al_2O_3$ and the H_2/CO ratio is *ca.* 7.5 as well. Following the same trends, conversion of glycerol remains nearly 100% and 97% for $PtO_x/MgO–Al_2O_3$ and $PtO_x/CeO_2–Al_2O_3$, respectively. In addition, the production of methane, carbon monoxide and carbon dioxide is negligible over both catalysts studied. Besides, the yield of H_2 and glycerol conversion becomes small over $PtO_x/CeO_2–Al_2O_3$ by using a space velocity of 0.5 h^{-1} while no change of the products distribution is observed.

Nevertheless, the activity of the catalysts differs depending upon whether more carbon deposition would form with increasing the time on stream. Thereby, it seems that unless coking can be removed on catalyst surface, a lesser hydrogen production would be observed on the solids. These results indicate superior catalytic properties in $PtO_x/MgO–Al_2O_3$ and appear to be attributed primarily to the ability of avoiding hard coking deposition. This data are further confirmed by spent catalysts characterization results. Moreover, the conversion of the solids is higher than that of unprompted 1 wt% Pt/Al_2O_3 catalyst.[1]

3.2. Characterizations of spent catalysts

3.2.1. XRD and Raman measurements. XRD patterns of the spent catalysts are shown in Fig. 2. All catalysts displays the main peaks at approximately 2θ equal to 33, 37, 49 and 68°, which corresponded, respectively to the (111), (220), (311), (400) and (440) planes of the R_3C type structure of γ-Al_2O_3 (JCPDS 46-1131). For $PtO_x/ZrO_2–Al_2O_3$, the diffraction pattern contains any peaks of ZrO_2 with tetragonal symmetry, belonging to $P4_2/nmc$ space group at around $2\theta = 30$, 35, 50, 60 and 74° regions of the XRD pattern. These peaks are indexed to be from (101), (002), (112), (211) and (200) reflexions and can be overlapped with those of alumina. Furthermore, the intensities of the peaks indicate that metal particles are too big to produce the aforesaid reflections. This observation is in agreement with the metal particle size of 35 nm for (002) plane of t-ZrO_2 as calculated from Scherer equation and also suggest sintering of the solid. No other characteristic peaks of platinum oxide phases eventually formed are detected owing to the superimposition with the aforesaid phases.

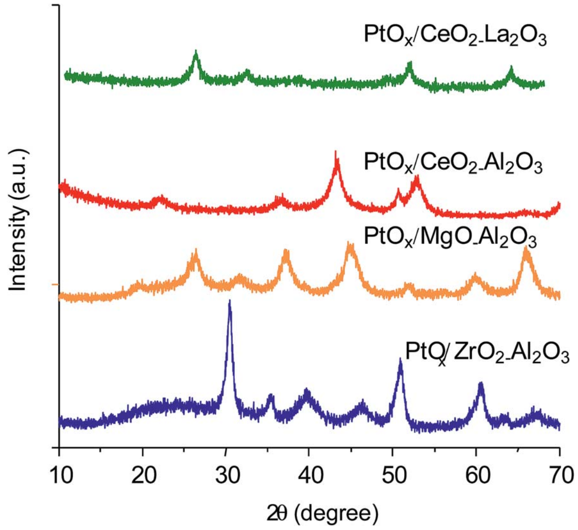

Fig. 2 XRD patterns of the spent catalysts after 5 h of time on stream in glycerol steam reforming.

In case of $PtO_x/MgO–Al_2O_3$, the broad diffraction peaks ascribable to cubic MgO (JCPDS 4-829) are present with reflexions at $2\theta = 42$ and 62°, respectively corresponding to (220) and (200) planes together with those of γ-Al_2O_3. Moreover, weak diffraction peaks of PtO_x species may be suggested, but they are at the same position of the $MgAl_2O_4$ at about $2\theta = 20$, 31, 37, 45, 56, 60 and 65°, corresponding to the reflexions of a $Fd\bar{3}m$ cubic spinel oxide (JCPDS-21-1152). Another possibility is that Pt particles are highly dispersed with the crystallite size beyond the detection limit of XRD. The findings states that during reforming of hydrocarbons reactions lead with Pt supported on $MgAl_2O_4$ catalysts, phase transformations of $MgAl_2O_4$ to MgO and γ-Al_2O_3, decrease the catalytic performance of the solid.[14] In addition, no diffraction peaks of metallic platinum are discernable over $PtO_x/ZrO_2–Al_2O_3$ and $PtO_x/MgO–Al_2O_3$, indicating that Pt could be highly dispersed. Graphite peak is also detected in small intense peaks around 2θ equal to 26 (002) and 44° (101). These assumptions suggest that sintering and phase transformations are the leading causes of the decrease of the catalytic performance of $PtO_x/ZrO_2–Al_2O_3$ at the beginning of the reaction; but this factor may not cause the deactivation of the solid. For $PtO_x/MgO–Al_2O_3$, all of these factors together with coking contribute do not decrease the hydrogen production.

Spent $PtO_x/CeO_2–Al_2O_3$ yields a broad diffraction pattern containing peaks at $2\theta = 34$ (111) and 55° (220) belonging to the $Fd\bar{3}m$ of cubic CeO_2. This pattern closely match the pattern for cubic fluorite type structure of CeO_2,[15,19] besides the aforesaid peaks of γ-Al_2O_3. Also, this pattern suggests the presence of an interaction between CeO_2 and Al_2O_3 to produce R_3-C cubic $CeAlO_3$ structure with the typical peak at 37° (110),[15] with the absence of unalloyed Pt and support. The presence of graphite phase at $2\theta = 25$ and 43° is consistent with the (002) (101) planes, which predicts the coexistence of carbonaceous deposits over the spent solid. Based on the Scherrer equation and the most intensive CeO_2 (111) diffraction peak, the average crystallite size of magnetite was estimated to be *ca.* 10 nm. Platinum peaks are not visible in the diffraction patterns probably due to the superimposition of the peaks. These facts accounts for a minor performance concerning to hydrogen yield of $PtO_x/CeO_2–Al_2O_3$, as compared to those of $PtO_x/ZrO_2–Al_2O_3$ and $PtO_x/MgO–Al_2O_3$.

The addition of La_2O_3 instead of Al_2O_3 on $PtO_x/CeO_2–La_2O_3$ seems to not change the XRD pattern comparing with spent $PtO_x/CeO_2–Al_2O_3$. This feature is attributed to the incorporation of the CeO_2 on lanthana framework forming a solid solution. The presence of the diffraction peaks at $2\theta = 35$ and 55° may be assigned to the (111) and (220) planes of CeO_2. Lanthana presence could be suggested at $2\theta = 26$ and 30°, which is assigned to hexagonal La_2O_3 (JCPDS 74-2430) but these reflexions appear in the same region of ceria; thereby, it is not possible to ascertain the presence of this oxide. Platinum phases are not seen, indicating a well-dispersed Pt structure on the surface of the support.

Crystallite size is calculated from X-ray line broadening of CeO_2 (111) using the Scherrer equation and the value is not obtained for $PtO_x/CeO_2–La_2O_3$ due to the broadness of the diffractogram. The slight intensity of the graphite observed for $PtO_x/CeO_2–La_2O_3$ at about at $2\theta = 26$ and 42° suggests that hard coking happened instead of crystal growth.

In addition, according to the JCPDS card number 01-1190, metallic platinum is commonly observed at around $2\theta = 39.8$ (111), 46.5 (200) and 67.8° (220). However, these peaks are not visible for all spent solids due to either overlap Pt peaks with those of the other phases or even the possible dispersion of Pt particles to undetectable sizes.

Glycerol has lower potential to form solid carbon in steam reforming reaction.[1] However, studies on Raman spectroscopy suggest that carbonaceous deposition is induced by some type of catalysts. To confirm this hypothesis, Raman spectra of the spent solids are shown in Fig. 3.

The shape and the broadness of the spectra of $PtO_x/CeO_2–La_2O_3$, $PtO_x/CeO_2–Al_2O_3$ and $PtO_x/MgO–Al_2O_3$, especially for vibrational modes at high wavenumbers confirm that carbonaceous deposits are formed during the catalytic runs. This interpretation is consistent with the fact that other studies have shown coking in steam reforming of hydrocarbons reaction over Pt or Ni-based catalysts.[21–23]

The appearance of a strong mode at around 460 cm^{-1} in $PtO_x/CeO_2–Al_2O_3$ means the F_{2g} mode of fluorite CeO_2 is clearly visible. In addition, the defects modes at around 610 cm^{-1} of Ce-based oxides[14,15] could not be detected due to its low intensity. This indicates that the phases such as CeO_2 and $CeAlO_3$ are present in the solid, in agreement with XRD results. At high frequencies, the Raman fingerprint of disordered Csp^2-based materials are found at around 1350 (D band) and 1585 cm^{-1} (G band) assigned to phonons of E_{2g} and A_{1g} symmetry, respectively. The D band is attributed to be caused by defects and disorder in the graphene-like structure whereas the G band is associated with the first-order scattering of the E_{2g} mode of in-plane sp^2 carbon single bond stretching vibrations from graphite sheets.[11,22,24,25] These modes definitely prove that disordered carbonaceous deposits always form on catalyst surface from C–C bond breakage of glycerol and their byproducts. Moreover, $PtO_x/CeO_2–La_2O_3$ spectrum shows the D′ band at about 1605–1620 cm^{-1}, which is due to the stretching of C=C bonds carbon of less structured coke or graphite-like structures.[24,25] In addition, two distinct broad modes with maxima at around 2652 and 2930 cm^{-1} are attributed to presence of defects, including the edges of the nanotubes in the so called G′ (or 2D) band.[26]

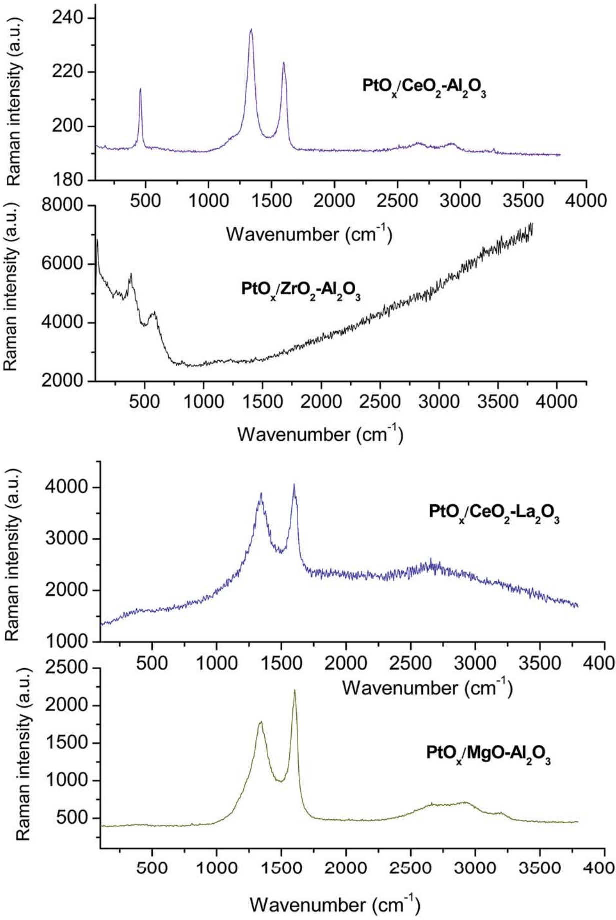

Fig. 3 Raman spectra of spent catalysts after 5 h of time on stream. Reaction conditions: fixed temperature (600 °C) and water to glycerol ratio of 9.

A comparison between $PtO_x/CeO_2–Al_2O_3$ and $PtO_x/CeO_2–La_2O_3$ spectra show distinct features concerning the intensity, position, and width of the modes. This suggest that deformation taking place in the crystal structure due to the larger ionic radius of La^{3+} compared to Ce^{4+} as well as the lattice expansion and the presence of oxygen vacancies over $PtO_x/CeO_2–La_2O_3$, as for Ce–La based catalysts applied to steam reforming of ethanol.[27] Literature reports that modes at around 350–400 cm^{-1} region are assumed to be from fundamental modes of La–O.[28] However, overlapping of the modes with those of CeO_2 does not allow lanthanum oxides identification. Besides, a hard carbon deposit on catalyst surface is considered a main cause of catalyst deactivation of $PtO_x/CeO_2–La_2O_3$, as already predicted by XRD.

Of similar features is the $PtO_x/MgO–Al_2O_3$ spectrum, which the G and D modes dominate the Raman spectrum together with an additional broad mode emerges at around 3227 cm^{-1} due to water presence.

The structural characterization of the deposited coke is taken from the intensity ratio of the I_D/I_G bands. According the findings, defects formation increases the I_D/I_G ratio but increases the I_{2D}/I_G ratio.[26] Noticeably, the ratio between the areas of the D and G bands of *ca.* 0.32 from $PtO_x/MgO–Al_2O_3$ indicates that the degree of graphitization of carbonaceous deposits greater than the other samples. Conversely, the D-to-G intensity ratio increases for 0.49 over $PtO_x/CeO_2–Al_2O_3$ in line with deposition of both low-graphitic coke with only few structural defects and amorphous carbonaceous deposits formation. Instead, deposition of amorphous carbon is observed for $PtO_x/CeO_2–La_2O_3$ with the I_D/I_G ratio of 0.57. Regarding the these results, the harsh coking from graphite type-carbon deposits accounts for the decrease performance of $PtO_x/MgO–Al_2O_3$ and $PtO_x/CeO_2–La_2O_3$ catalysts whereas correspondingly amorphous coke formation may be smoothly removed by steam and this not diminish $PtO_x/MgO–Al_2O_3$ performance. It may be possible that this kind of coke may be from the formation of olefinic chains and aromatic rings, as for magnesia and alumina-based catalysts tested in glycerol steam reforming.[21]

Raman spectrum of $PtO_x/ZrO_2–Al_2O_3$ displays modes at around 319 (E_g), and 634 cm^{-1} (B_{1g}) due to tetragonal ($P4_2/nmc$ (${D_{4h}}^{15}$) space group) and monoclinic ($P2_1/c$ (${C_{2h}}^{5}$) space group) phases of ZrO_2.[29] This means that the typical of both tetragonal and monoclinic ZrO_2 phases are present in the in segregated phases confirming the hypothesis of sintering of the solid after the catalytic test. A strong luminescence caused by alumina impedes the other modes identification. It is most likely that $PtO_x/ZrO_2–Al_2O_3$ is deactivated by phase transformation and sintering instead of carbon deposition, since carbon modes are not visible by Raman spectroscopy.

3.2.2. TEM and Surface texture of the solids.

TEM images of the spent catalysts are shown in Fig. 4.

It can be seen that the spent $PtO_x/CeO_2–Al_2O_3$ (Fig. 4a$_1$) exhibits the characteristic rod-like carbon morphology, similar to that of carbon nanotubes. The value of *d* spacing of *ca* 0.225 nm, from (111) plane as well as dispersed black spots, confirm the Pt nanoparticles remains intact after the catalytic test and possess varying between 5 to 12 nm. In addition, these nanoparticles are in a well dispersed fashion and the nanoparticles sizes values close to that obtained XRD results. It is further illustrated the presence of typical carbonaceous deposits formation in Fig. 4b$_1$. Filamentous and carbon nanotubes formation are likely on the spent solid. Moreover, nanoscale Pt metal particles possessing diameters ranging from 0.5 to 2 nm are very evident inside the tubes along with amorphous carbon (Fig. 4a$_1$). It might be possible that on $PtO_x/CeO_2–Al_2O_3$ surface, the decomposition of glycerol and the subsequent layers of carbonaceous species deposition start to form on Pt sites of active metals for shorter duration; however, a slight hindrance of the activity of the solid is observed due to carbon gasification towards CO_2 formed during the reaction, as observed in the catalytic results.

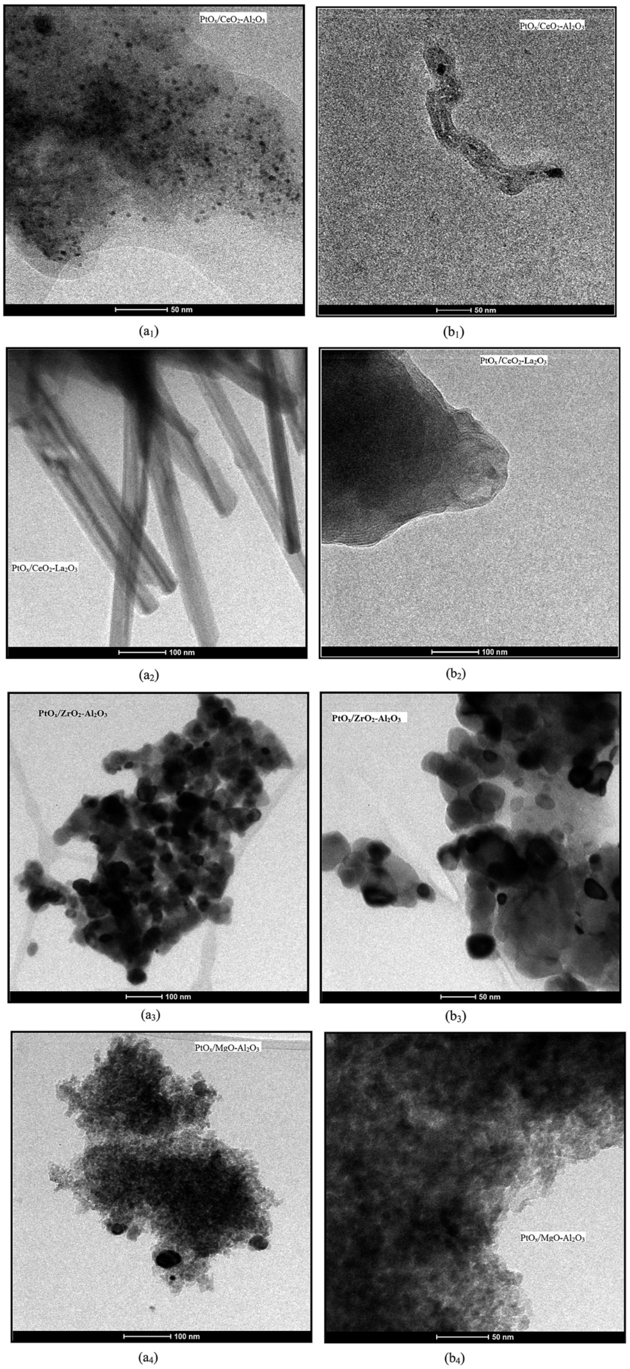

Fig. 4 (a) TEM and HRTEM images of the spent catalysts, after 5 h on stream in steam reforming of glycerol and water to glycerol molar ratio of 9 at 600° C.

TEM micrograph of PtO_x/CeO_2–La_2O_3 (Fig. 4a$_2$) illustrates domains possessing a high degree of crystallinity resulting in a needle-like structure and a corrugated surface with repeating ridges. HRTEM image (Fig. 4b$_2$) displays transparent carbon sheets with crumpled silk veil waves and the rumples are involved by the Pt nanoparticles, which has an average size of approximately 6–18 nm. In addition, fringes of several crystallites in different orientations can be seen from an electron diffraction pattern including the layered carbon nanostructures. Also, the crystal lattice fringes reveal that these particles are from highly crystalline features of Pt. These features suggest that deactivation of PtO_x/CeO_2–La_2O_3 is mainly due to coking in agreement with previous Raman and XRD results. The Ce–La solid solution formation is formed during the catalytic test consisting with the results based on literature.[27] This might be induced further a crystal growth and thereby, formation of the aforesaid crystal type-structure results in a low performance of the solid in the steam reforming of glycerol reaction. Additionally, the findings states that carbon species formed on metallic sites may be partially removed by oxygen species originating from lanthanum carbonate species such as $La_2O_2CO_3$.[7] However, this phenomenon is not observed for PtO_x/CeO_2–La_2O_3, judging from its low performance in the reaction.

It is clearly seen that the TEM image of PtO_x/ZrO_2–Al_2O_3 (Fig. 3a$_3$) exhibits large particles occupying almost of the entire of solid surface. These particles are indeed densely aggregated with fairly even distribution (Fig. 3b$_3$), which indicate the strong interaction between the Pt nanoparticles and the ZrO_2–Al_2O_3. The characteristics of a crystalline Pt face centred cubic structure is confirmed by *d*-spacings of the lattice fringes at around 0.225 nm, which can be indexed to as the (111) crystalline plane of Pt.[30] The lattice distances of the Al_2O_3 obtained from high-resolution TEM (HRTEM) image (*e.g.*, 0.7 nm) and t-ZrO_2 (belonging to the $P4_2/nmc$ space group possessing $d = 0.284$ nm from (111) planes with JCPDS number card 37-1484) are clearly visible. The particles particle sizes obtained are estimated to be 39 nm, in average and this is in coherence with the data obtained from XRD patterns. From these results, it can be confirmed that the cause of deactivation of PtO_x/ZrO_2–Al_2O_3 catalyst is sintering of Pt particles and phase transformations.

Based on TEM measurements of PtO_x/MgO–Al_2O_3 (Fig. 4a$_4$), agglomeration of Pt particles in random regions with an average particle size of 10–30 nm is observed. The edges of the particles area are all surrounded by carbonaceous species, which are supposed to be from carbon whiskers fibers formed during the glycerol steam reforming tests (Fig. 4b$_4$). Although some metal particles encapsulated within the filaments could help the side WGS reaction and carbon formation with an auto consumption process during reforming process,[31] coke formation together with sintering contributes to decrease the catalytic properties of the solid, which is consistent with the XRD and Raman results.

Table 1 displays the textural properties of spent catalysts. The fresh catalysts are mesoporous materials that possess elevated textural properties.[17] It seems that some of the catalyst pores might have suffered by sintering and carbonaceous deposits formation on solid surface and thus, affecting the textural properties.

Contrary to the abovementioned expectation, the unchanged surface area of *ca.* 83 $m^2\ g^{-1}$ and pore volume of *ca.* 0.12 $cm^3\ g^{-1}$ registered for PtO_x/CeO_2–Al_2O_3 may be attributed to a lesser intensity of the catalytic deactivation, probably. This implied that carbon entities formed on spent catalyst neither occupy the active sites nor cover the Pt site, consequently these fact did not impair the activity of the solid. BET surface, pore volume and pore size of the other samples decrease after catalytic evaluation. It is noted that surface area is reduced from 143 $m^2\ g^{-1}$ for the fresh PtO_x/ZrO_2–Al_2O_3 to 73 $m^2\ g^{-1}$, which is considered to be a drastic reduction due to sintering effects, as observed previously by the other characterization techniques. In case of PtO_x/MgO–Al_2O_3, the textural properties remain almost unaltered, thereby, it can be regarded that coking is eliminated on the solid surface as soon as it is formed and this accounts for the best catalytic properties of the solid. For PtO_x/CeO_2–La_2O_3, a drop of the BET surface area and pore volume is observed compared to the fresh solid, suggesting the coke is not vanished from solid surface resulting in a low catalytic performance of the solid. The pore diameter of the spent catalyst is adequate (2.8–4.5 nm) to allow the reforming reaction occurring inside the inner channels because it was much greater than the size of glycerol molecule which is around 0.62 nm^3. Even if the pores of PtO_x/CeO_2–Al_2O_3 and PtO_x/ZrO_2–Al_2O_3 experience a decreased due to sintering, it is likely that deactivation may be not due to the diffusion limitation of the reactants or products.

3.2.3. SEM-EDS and TG analyses. Fig. 5 exhibits the SEM-EDS micrographs of the spent solids. It seems that the morphology of spent PtO_x/CeO_2–La_2O_3 (Fig. 5a$_1$) consists of coke deposits in which nanofibers are noticed. Elemental maps of the main elements such as Pt, Al, Ce, La and C from the sample area suggest a heterogeneous distribution of carbon on solid surface. According to the above Raman, TEM and XRD predictions, the carbonaceous deposits (both amorphous and graphitic) on solid surface is the main cause of the lesser performance of PtO_x/CeO_2–La_2O_3 to hydrogen production from steam reforming of glycerol. SEM micrograph of PtO_x/CeO_2–Al_2O_3 suggests the formation of aggregates of nanoparticles, probably from the segregated CeO_x island. Nevertheless, this could be a moderate accumulation of CeO_x particles, as proved previously by TEM image of the solid. The corresponding EDS spectrum (Fig. 5a$_2$), a quite uniform distribution of Pt and Al is observed, besides the expected carbon presence, which tends to be accumulated on spent PtO_x/CeO_2–Al_2O_3 surface.

As seen from SEM image of PtO_x/MgO–Al_2O_3, the solid surface is composed of very bulky spherical-like particles. These particles are coated by a carbon layer in which carbon fibers and carbon nanotubes are observed, as indicated previously by Raman spectroscopy. As EDS spectrum suggests an homogeneous distribution of Al, Mg and Pt elements, it would be indicated that carbon deposition does not cover the active sites and the morphological and textural properties of the solid remains unaltered. This is also observed for Ni-based catalysts in the glycerol steam reforming[31,32] and coking do not damage the catalytic performance of the solid.

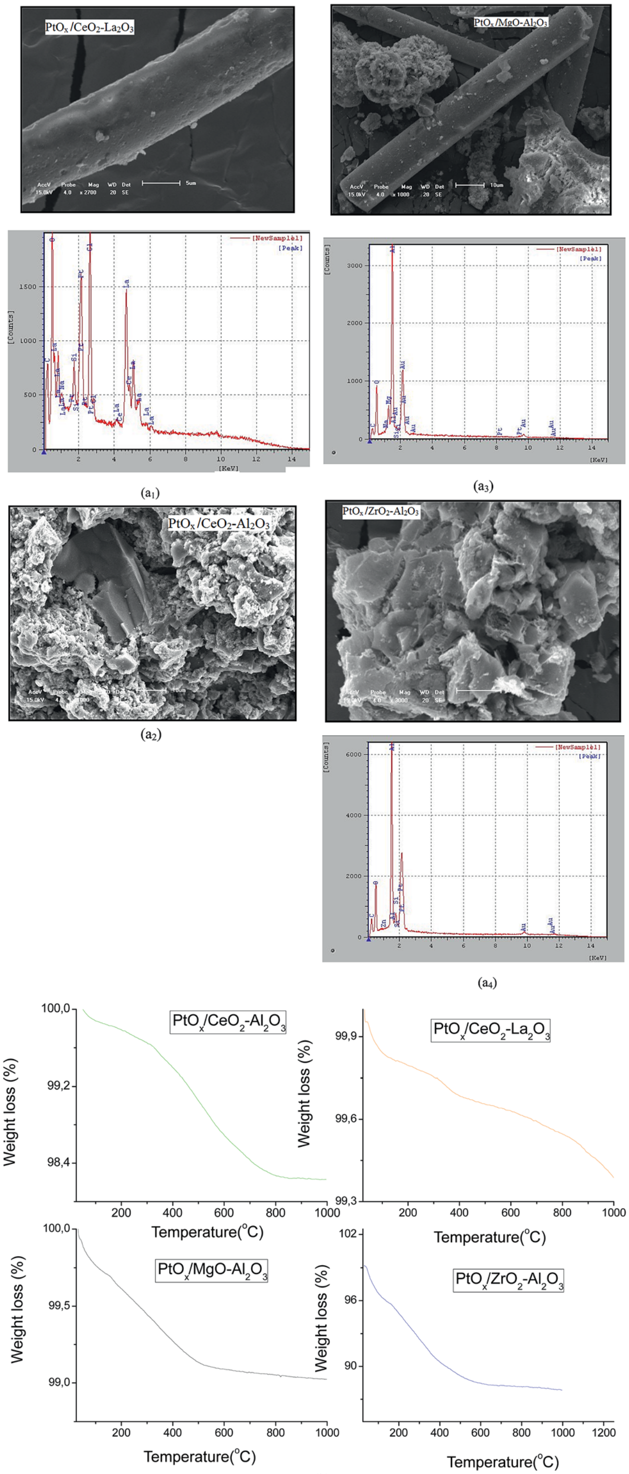

(a₁) (a₃) (a₂) (a₄) (b)

Fig. 5 (a) SEM-EDS of the solids after the catalytic test (b) TG of spent solids.

SEM image of $PtO_x/ZrO_2–Al_2O_3$ shows the sintering of the particles of after reaction, since aggregation of particles is noted. The EDS spectrum of the solid displays the signals of the main elements such as Zr, Al, Pt and C, in which the content of the latter is too low and any kind of heterogeneity of the composition is definitely shown.

TG analysis of $PtO_x/CeO_2–La_2O_3$ after catalytic run reveals the occurrence of a mass loss in the first step (25–150 °C), which is assigned to removal of adsorbed water. A subsequent significant mass loss is observed in the 150–350 °C is due to the elimination of interstitial water and combustion of amorphous carbonaceous species originated from glycerol decomposition to other organic by-products that can be adsorbed on the surface covering the active sites, and in some extent blocking the catalyst pores.[4] The IR curves from TG experiments are included in ESI.† According to the findings, amorphous carbon oxidizes below 550 °C whereas graphitic/filamentous carbon does at higher temperature.[33] The third weight loss event, with a highest mass loss is observed at around 400–800 °C, being ascribed to the graphitic carbon elimination at elevated temperatures. As reported in the literature,[33] under steam reforming conditions, coking gasification is promoted by water in steam reforming reactions. This could indeed result in structural defects, such as vacancies, face edges and among others defects on the solid. With this in mind, the weight loss of *ca.* 1% on $PtO_x/CeO_2–La_2O_3$ might be result of previous coking removal by steam and oxidation of CeO_2 to create such defects could be likely.

A comparison between $PtO_x/CeO_2–La_2O_3$ and $PtO_x/CeO_2–Al_2O_3$ curves shows that the weight loss of the latter is divided in two events. The first one is observed at around 25–350 °C temperature range, which is ascribed to the removal of interstitial water and/or the oxidation of the amorphous carbonaceous species, as previously suggested by Raman spectroscopy. The second event peak is very wide and oxidation of carbon deposits take place in the 300–700 °C, and overlaps graphitic carbonaceous species oxidation and re-oxidation oxidation of CeO_2 and Pt atoms. The 2% amount of coke deposited on the solid is a result of the formation rate minus the gasification rate, which accounts for the lower coke amount found on $PtO_x/CeO_2–Al_2O_3$, in agreement with SEM-EDS results.

TG curve of spent $PtO_x/MgO–Al_2O_3$ shows only one weight loss event that occurred at around 25–400 °C is due to the formed coke elimination at lower temperatures. It has being stated that Mg and Ca incorporation to catalysts can enhance the steam gasification of coke by activating water adsorption[33] and thus, this accounts for the better performance of this solid, even if graphite carbon is majoritary formed during SR (Raman spectroscopy). The TG curve of $PtO_x/ZrO_2–Al_2O_3$ does not seem to undergo any difference concerning the unique event observed. However, it might be a result of the evaporation of occluded water and the oxidation of the aggregated particle, since a low amount of coke is deposited on the solid surface. These results are consistent with those obtained by SEM-EDS and Raman analyses.

4. Conclusions

Pt-containing $MeO_x–Al_2O_3$ catalysts were evaluated in glycerol steam reforming. Using MgO and CeO_2 promoters, the solids had elevated glycerol conversions and selectively produced hydrogen with low yields to byproducts whereas La_2O_3 and ZrO_2 promoters were found to be lesser selectives to hydrogen production. Spent catalysts characterizations by Raman, TEM, XRD, TG and SEM-EDS as well as textural properties techniques showed that coking, rather than sintering is the main cause that determine the low hydrogen selectivity of the solids. The coking did not cover the active sites of Pt/MgO–Al_2O_3 and Pt/CeO_2–Al_2O_3 and steam suppress carbon deposition, and thus improve the catalyst stability in steam reforming of glycerol.

Acknowledgements

The financial supports of this work by CNPq with contract no. 490162/2011-8 and Funcap (areas estrategicas 2011 project) are gratefully acknowledged. We would like to thank CETENE-INT for TEM measurements as well as Dr A. J de Paula for SEM-EDS analyses at Central Analitica da UFC.

References

1 N. H. Tran and G. S. Kamali Kannangar, *Chem. Soc. Rev.*, 2013, **42**, 9454.

2 L. P. R. Profeti, E. A. Ticianelli and E. M. Assaf, *Int. J. Hydrogen Energy*, 2009, **34**, 5049.

3 S. Li and J. Gong, *Chem. Soc. Rev.*, 2014, **43**, 7245–7256.

4 G. Sadanandam, K. Ramya, D. B. Kishore, V. Durgakumari, M. Subrahmanyam and K. V. R. Chary, *RSC Adv.*, 2014, **4**, 32429.

5 T. A. Maia and E. M. Assaf, *RSC Adv.*, 2014, **4**, 31142.

6 G. Wu, S. Li, C. Zhang, T. Wang and J. Gong, *Appl. Catal., B*, 2014, **144**, 277.

7 V. V. Thyssen, T. A. Maia and E. M. Assaf, *Fuel*, 2013, **105**, 358.

8 T. Montini, R. Singh, P. Das, B. Lorenzut, N. Bertero, P. Riello, A. Benedetti, G. Giambastiani, C. Bianchini, S. Zinoviev, S. Miertus and P. Fornasiero, *ChemSusChem*, 2010, **3**, 619.

9 C. D. Dave and K. K. Pant, *Renewable Energy*, 2011, **36**, 3195.

10 A. Iriondo, V. Barrio, J. Cambra, P. Arias, M. Guemez, M. Sanchez, R. Navarro and J. L. Fierro, *Int. J. Hydrogen Energy*, 2010, **35**, 11622.

11 M. M. Rahman, T. L. Church, M. F. Variava, A. T. Harris and A. I. Minett, *RSC Adv.*, 2014, **4**, 18951.

12 I. Rossetti, J. Lasso, V. Nichele, M. Signoretto, E. Finocchio, G. Ramis and A. Di Michele, *Appl. Catal., B*, 2014, **150–151**, 257.

13 E. L. Kunkes, D. A. Simonetti, J. A. Dumesic, W. D. Pyrz, L. E. Murillo, J. G. Chen and D. J. Buttrey, *J. Catal.*, 2008, **260**, 164.

14 H. S. A. de Sousa, A. N. da Silva, A. J. R. Castro, A. Campos, J. M. Filho and A. C. Oliveira, *Int. J. Hydrogen Energy*, 2012, **37**, 12281.

15 F. F. de Sousa, H. S. A. de Sousa, A. C. Oliveira, M. C. C. Junior, A. P. Ayala, E. B. Barros, B. C. Viana, J. M. Filho and A. C. Oliveira, *Int. J. Hydrogen Energy*, 2012, **37**, 3201.

16 K. Seung-hoon, J. Jae-sun, Y. Eun-hyeok, L. Kwan-Young and M. D. Ju, *Catal. Today*, 2014, **228**, 145.

17 D. C. Carvalho, H. S. A. De Souza, J. M. Filho, A. C. Oliveira, A. Campos, É. R. C. Milet, F. F. de Sousa, E. P. Hernández and A. C. Oliveira, *Appl. Catal., A*, 2014, **473**, 132.

18 C. A. Franchini, W. Aranzaez, A. M. Duarte de Farias, G. Pecchi and M. A. Fraga, *Appl. Catal., B*, 2014, **147**, 193.

19 P. Pantu and G. R. Gavalas, *Appl. Catal., A*, 2002, **223**, 253.

20 J. W. Shabaker, R. R. Davd, G. W. Huber, R. D. Cortright and J. A. Dumesic, *J. Catal.*, 2003, **215**, 344.

21 B. Valle, B. Aramburu, A. Remiro, J. Bilbao and A. G. Gayubo, *Appl. Catal., B*, 2014, **147**, 402.

22 M. El Doukkali, A. Iriondo, P. L. Arias, J. F. Cambra, I. Gandarias and V. L. Barrio, *Int. J. Hydrogen Energy*, 2012, **37**, 8298.

23 L. He, J. M. S. Parra, E. A. Blekkan and D. Chen, *Energy Environ. Sci.*, 2010, **3**, 1046.

24 A. Serrano-Lotina and L. Daza, *Appl. Catal., A*, 2014, **474**, 107.

25 W. Donphai, K. Faungnawakij, M. Chareonpanich and J. Limtrakul, *Appl. Catal., A*, 2014, **475**, 16.

26 A. O. Al-Youbi, J. L. Gómez de la Fuente, F. J. Pérez-Alonso, A. Y. Obaid, J. L. G. Fierro, M. A. Peña, M. Abdel Salam and S. Rojas, *Appl. Catal., B*, 2014, **150–151**, 21.

27 X. Han, Y. Yu, H. He and W. Shan, *Int. J. Hydrogen Energy*, 2013, **38**, 10293.

28 B. M. Faroldi, J. F. Múnera and L. M. Cornaglia, *Appl. Catal., B*, 2014, **150–151**, 126.

29 R. Pazhani, H. P. Kumar, A. Varghese, A. M. E. Raj, S. Solomon and J. K. Thomas, *J. Alloys Compd.*, 2011, **509**, 6819–6823.

30 M. Zhang, J. Xie, Q. Sun, Z. Yan, M. Chen and J. Jing, *Int. J. Hydrogen Energy*, 2013, **38**, 16402.

31 J. Segner, C. T. Campbell, G. Doyen and G. Ertl, Catalytic oxidation of CO on Pt (111): the influence of surface defects and composition on the reaction dynamics, *Surf. Sci.*, 1984, **138**, 505.

32 L. F. Bobadilla, A. Álvarez, M. I. Domínguez, F. Romero-Sarria, M. A. Centeno, M. Montes and J. A. Odriozola, *Appl. Catal., B*, 2012, **123–124**, 379.

33 J. A. Calles, A. Carrero, A. J. Vizcaíno and L. García-Moreno, *Catal. Today*, 2014, **227**, 198.